Supplementary Information

Synthesized complex-frequency excitation for ultrasensitive molecular sensing

Kebo Zeng[1]†, Chenchen Wu[2]†, Xiangdong Guo[1,2]†, Fuxin Guan [1]†, Yu Duan[2], Lauren L Zhang[3], Xiaoxia Yang[2]*, Na Liu[4]*, Qing Dai[2]* and Shuang Zhang[1,5]*

[1]New Cornerstone Science Laboratory, Department of Physics, University of Hong Kong, Hong Kong, China

[2]CAS Key Laboratory of Nanophotonic Materials and Devices, CAS Key Laboratory of Standardization and Measurement for Nanotechnology, CAS Center for Excellence in Nanoscience, National Center for Nanoscience and Technology, Beijing, China

[3]Department of Chemistry & Chemical Biology, Harvard University, Cambridge, MA 02138, USA

[4]2nd Physics Institute, University of Stuttgart, Pfaffenwaldring 57, 70569, Stuttgart, Germany

[5]Department of Electrical & Electronic Engineering, University of Hong Kong, Hong Kong, China

† These authors contributed equally to this work.

*Corresponding author: yangxx@nanoctr.cn, na.liu@pi2.uni-stuttgart.de, daiq@nanoctr.cn, shuzhang@hku.hk

Note 1. Synthesized CFW error and its reduction by time-average

For an ideal truncated CFW which is expressed as $\mathrm{e}^{-i\tilde{\omega}t_0}\theta(t_0)$, the amplitude jumps from 0 to 1 at $t_0 = 0$ and decays exponentially over time. Due to the truncation, the system cannot reach a quasi-steady state instantaneously at $t_0 = 0$, but gradually approaches the quasi-steady state after a sufficient period of relaxation. Here we will show that the truncation causes some side bands for each resonance, whose effect can be minimized via time-average. In addition, in actual calculation, limited frequency range and discretized frequency points will also contribute to certain level of error. Specifically, during the decay of the amplitude over time, the influence of the finite frequency range becomes more and more significant, increasing the instability of synthesized CFW.

We first look into the effect of truncation and finite frequency range, while overlooking the influence of discretization at the moment. We start with the simplest case, a molecular system with a single resonance with resonance frequency ω_0 and dissipation γ. To further simplify the derivation, we use an approximate formulation of the Lorentzian resonance for the susceptibility of the molecules: $\chi(\omega) = \frac{A}{\omega_0 - \omega - \mathrm{i}\gamma} = \frac{A}{\tilde{\omega}_0 - \omega}$, where γ correspond to $\gamma_\mathrm{M}/2$ in equation (1) of the main text, and $\tilde{\omega}_0 \equiv \omega_0 - \mathrm{i}\gamma$. Using the integral form of the expansion of susceptibility under complex excitation we have,

$$\begin{aligned}\chi(\tilde{\omega}, t_0) &\approx \frac{1}{2\pi}\int_\alpha^\beta \frac{\chi(\omega')}{\mathrm{i}(\tilde{\omega} - \omega')}\mathrm{e}^{\mathrm{i}(\tilde{\omega}-\omega')t_0}\mathrm{d}\omega' \\ &= \frac{1}{2\pi\mathrm{i}}\int_\alpha^\beta \frac{A}{(\tilde{\omega}_0 - \omega')}\frac{1}{(\tilde{\omega} - \omega')}\mathrm{e}^{\mathrm{i}(\tilde{\omega}-\omega')t_0}\mathrm{d}\omega' \\ &= \frac{A}{2\pi\mathrm{i}(\tilde{\omega}_0 - \tilde{\omega})}\int_\alpha^\beta \left(\frac{1}{\tilde{\omega} - \omega'} - \frac{1}{\tilde{\omega}_0 - \omega'}\right)\mathrm{e}^{\mathrm{i}(\tilde{\omega}-\omega')t_0}\mathrm{d}\omega'\end{aligned}$$

where α and β are the lower and upper limit of the frequency range. The above integration can be solved as,

$$\begin{aligned}\chi(\tilde{\omega}, t_0) \approx \frac{A}{2\pi\mathrm{i}(\tilde{\omega}_0 - \tilde{\omega})}\big[&(E_1[\mathrm{i}(\beta - \tilde{\omega})t_0] - E_1[\mathrm{i}(\alpha - \tilde{\omega})t_0] + 2\pi\mathrm{i}) \\ &- (E_1[\mathrm{i}(\beta - \tilde{\omega}_0)t_0] - E_1[\mathrm{i}(\alpha - \tilde{\omega}_0)t_0] + 2\pi\mathrm{i})\mathrm{e}^{\mathrm{i}(\tilde{\omega}-\tilde{\omega}_0)t_0}\big]\end{aligned} \tag{S1}$$

where $E_1[x] = \int_x^\infty \frac{\mathrm{e}^{-u}}{u}\mathrm{d}u$ is the exponential integral function. In the large frequency

range limit $\alpha \to -\infty,\ \beta \to +\infty$, the above equation can approach,

$$\chi(\widetilde{\omega}, t_0) \approx \frac{A}{(\widetilde{\omega}_0 - \widetilde{\omega})}\left[1 - \mathrm{e}^{\mathrm{i}(\widetilde{\omega}-\widetilde{\omega}_0)t_0}\right] \tag{S2}$$

Compared to the real expression of susceptibility under complex frequency excitation, the above equation contains an additional exponential term (second term on the right side), which is caused by the truncation of the complex frequency signal. This additional exponential term leads to the presence of sidebands around the main Lorentzian peak, as shown by Fig. S1a. It is noticed that the frequencies of the side bands vary with t_0, and therefore by performing a time average across a finite range of t_0, the effect of the sidebands can be smoothed out.

For the case of coupling of the molecular resonance to the plasmonic resonance of graphene, we consider the following coupled equations between the molecular and the graphene responses,

$$(\omega - \omega_a + \mathrm{i}\gamma_a)a + \kappa b = -g_a E \tag{S3}$$

$$(\omega - \omega_b + \mathrm{i}\gamma_b)b + \kappa a = -g_b E \tag{S4}$$

where ω_a, ω_b are the resonance frequencies of the molecule and the graphene antenna, respectively, and γ_a and γ_b are the corresponding dissipation rates, κ is the coupling coefficient between the molecules and the graphene, g_a and g_b are the parameters indicating how strong each resonance couples with the incident electromagnetic wave, and generally we have $g_b \gg g_a$, i.e. the graphene antennas couple much stronger with the incident electromagnetic wave than the molecules. Let $\delta_a = \omega - \omega_a$ and $\delta_b = \omega - \omega_b$, and neglect g_a,

$$\begin{pmatrix} \delta_a + \mathrm{i}\gamma_a & \kappa \\ \kappa & \delta_b + \mathrm{i}\gamma_b \end{pmatrix}\begin{pmatrix} a \\ b \end{pmatrix} = -\begin{pmatrix} 0 \\ g_b E \end{pmatrix} \tag{S5}$$

The susceptibility of the combined system is dominated by the graphene response, which is given by,

$$\chi \propto b/E = \frac{-g_b(\delta_a + \mathrm{i}\gamma_a)}{(\delta_a + \mathrm{i}\gamma_a)(\delta_b + \mathrm{i}\gamma_b) - \kappa^2} \tag{S6}$$

Let $\widetilde{\omega}_a = \omega_a - \mathrm{i}\gamma_a,\ \widetilde{\omega}_b = \omega_b - \mathrm{i}\gamma_b$,

$$-\frac{\chi}{g_b} = \frac{\omega - \widetilde{\omega}_a}{\omega^2 - (\widetilde{\omega}_a + \widetilde{\omega}_b)\omega + (\widetilde{\omega}_a\widetilde{\omega}_b - \kappa^2)} = \frac{\omega - \widetilde{\omega}_a}{(\omega - \widetilde{\omega}_1)(\omega - \widetilde{\omega}_2)}$$

where $\widetilde{\omega}_1 = \frac{\widetilde{\omega}_a + \widetilde{\omega}_b + \sqrt{(\widetilde{\omega}_a - \widetilde{\omega}_b)^2 + 4\kappa^2}}{2}$, $\widetilde{\omega}_2 = \frac{\widetilde{\omega}_a + \widetilde{\omega}_b - \sqrt{(\widetilde{\omega}_a - \widetilde{\omega}_b)^2 + 4\kappa^2}}{2}$ are the hybridized complex resonance frequencies of the coupled system. The above equation can be

rewritten as,

$$-\frac{\chi}{g_b}=\frac{1}{(\widetilde{\omega}_1-\widetilde{\omega}_2)}(\frac{\widetilde{\omega}_1-\widetilde{\omega}_a}{\omega-\widetilde{\omega}_1}-\frac{\widetilde{\omega}_2-\widetilde{\omega}_a}{\omega-\widetilde{\omega}_2}) \tag{S7}$$

Then it can be rewritten as,

$$\chi=A(\frac{\widetilde{\omega}_1-\widetilde{\omega}_a}{\omega-\widetilde{\omega}_1}-\frac{\widetilde{\omega}_2-\widetilde{\omega}_a}{\omega-\widetilde{\omega}_2}) \tag{S8}$$

where $A=-\frac{g_b}{(\widetilde{\omega}_1-\widetilde{\omega}_2)}$. Using S4, we obtain,

$$\chi(\widetilde{\omega},t_0)\approx\frac{A}{2\pi\mathrm{i}}\int_\alpha^\beta\frac{\mathrm{e}^{\mathrm{i}(\widetilde{\omega}-\omega')t_0}}{(\widetilde{\omega}-\omega')}(\frac{\widetilde{\omega}_1-\widetilde{\omega}_a}{\omega-\widetilde{\omega}_1}-\frac{\widetilde{\omega}_2-\widetilde{\omega}_a}{\omega-\widetilde{\omega}_2})\mathrm{d}\omega'$$

Based on the derivation of single resonance, one can obtain the results for coupled resonance,

$$\begin{aligned}\chi(\widetilde{\omega},t_0)\approx&\frac{A(\widetilde{\omega}_1-\widetilde{\omega}_a)}{2\pi\mathrm{i}(\widetilde{\omega}-\widetilde{\omega}_1)}\big[(E_1[\mathrm{i}(\beta-\widetilde{\omega})t_0]-E_1[\mathrm{i}(\alpha-\widetilde{\omega})t_0]+2\pi\mathrm{i})\\&-(E_1[\mathrm{i}(\beta-\widetilde{\omega}_1)t_0]-E_1[\mathrm{i}(\alpha-\widetilde{\omega}_1)t_0]+2\pi\mathrm{i})\mathrm{e}^{\mathrm{i}(\widetilde{\omega}-\widetilde{\omega}_1)t_0}\big]\\&-\frac{A(\widetilde{\omega}_2-\widetilde{\omega}_a)}{2\pi\mathrm{i}(\widetilde{\omega}-\widetilde{\omega}_2)}\big[(E_1[\mathrm{i}(\beta-\widetilde{\omega})t_0]-E_1[\mathrm{i}(\alpha-\widetilde{\omega})t_0]+2\pi\mathrm{i})\\&-(E_1[\mathrm{i}(\beta-\widetilde{\omega}_2)t_0]-E_1[\mathrm{i}(\alpha-\widetilde{\omega}_2)t_0]+2\pi\mathrm{i})\mathrm{e}^{\mathrm{i}(\widetilde{\omega}-\widetilde{\omega}_2)t_0}\big]\end{aligned} \tag{S9}$$

Similar to the case of single resonance, at the large frequency range limit $\alpha\to-\infty$, $\beta\to+\infty$, the above equation can be approximated as,

$$\chi(\widetilde{\omega},t_0)\approx\frac{A(\widetilde{\omega}_1-\widetilde{\omega}_a)}{(\widetilde{\omega}-\widetilde{\omega}_1)}\big(1-\mathrm{e}^{\mathrm{i}(\widetilde{\omega}-\widetilde{\omega}_1)t_0}\big)-\frac{A(\widetilde{\omega}_2-\widetilde{\omega}_a)}{(\widetilde{\omega}-\widetilde{\omega}_2)}\big(1-\mathrm{e}^{\mathrm{i}(\widetilde{\omega}-\widetilde{\omega}_2)t_0}\big) \tag{S10}$$

Similarly, two additional exponential terms in the above equation cause the presence of sidebands around the resonances, as shown by Fig. S1e.

We next investigate the combined effect of finite frequency range and finite frequency interval, which cause deviation of the synthesized CFW from an ideal truncated CFW. Due to the discretization of frequency, $\chi(\widetilde{\omega},t_0)$ has no analytical solution but has to be numerically evaluated by $\chi(\widetilde{\omega},t_0)\approx\sum_n\chi(\omega_n)\frac{1}{\mathrm{i}(\widetilde{\omega}-\omega_n)}\mathrm{e}^{\mathrm{i}(\widetilde{\omega}-\omega_n)t_0}\Delta\omega/2\pi$. Fig. S1b and Fig. S1f show that at large t_0, the oscillation of $\chi(\widetilde{\omega},t_0)$ become unstable, leading to breakdown of the quasi-steady state of the system. Fig. S1c-d and Fig. S1g-h show that increasing the frequency range and reducing the frequency interval can help reduce the oscillation error and prolong the quasi-steady state duration. In order to

reduce the error, one can take the time average of $\chi(\tilde{\omega}, t_0)$ across suitably chosen time intervals, as shown in Fig. S1i-j.

$P(\tilde{\omega})$ calculated by equation (6) suffers from similar error and instability, as shown by Fig. S2a. We show that compared with the extinction $I(\tilde{\omega})$ obtained by $P(\tilde{\omega})$ at $t_0 = 8$ ns (the blue curve in Fig. S3b), $I(\tilde{\omega})$ calculated by the time-average of $P(\tilde{\omega})$ (the red curve in Fig. S2b) is more stable and smoother. This method is also valid for the experimental results. As an example, we show the time-average of $P(\tilde{\omega}, t_0)$ of the experimental result of BSA protein layer measured by GP-based sensor, as shown in Fig. S2c-d, which exhibit significantly reduced oscillatory features of the sidebands.

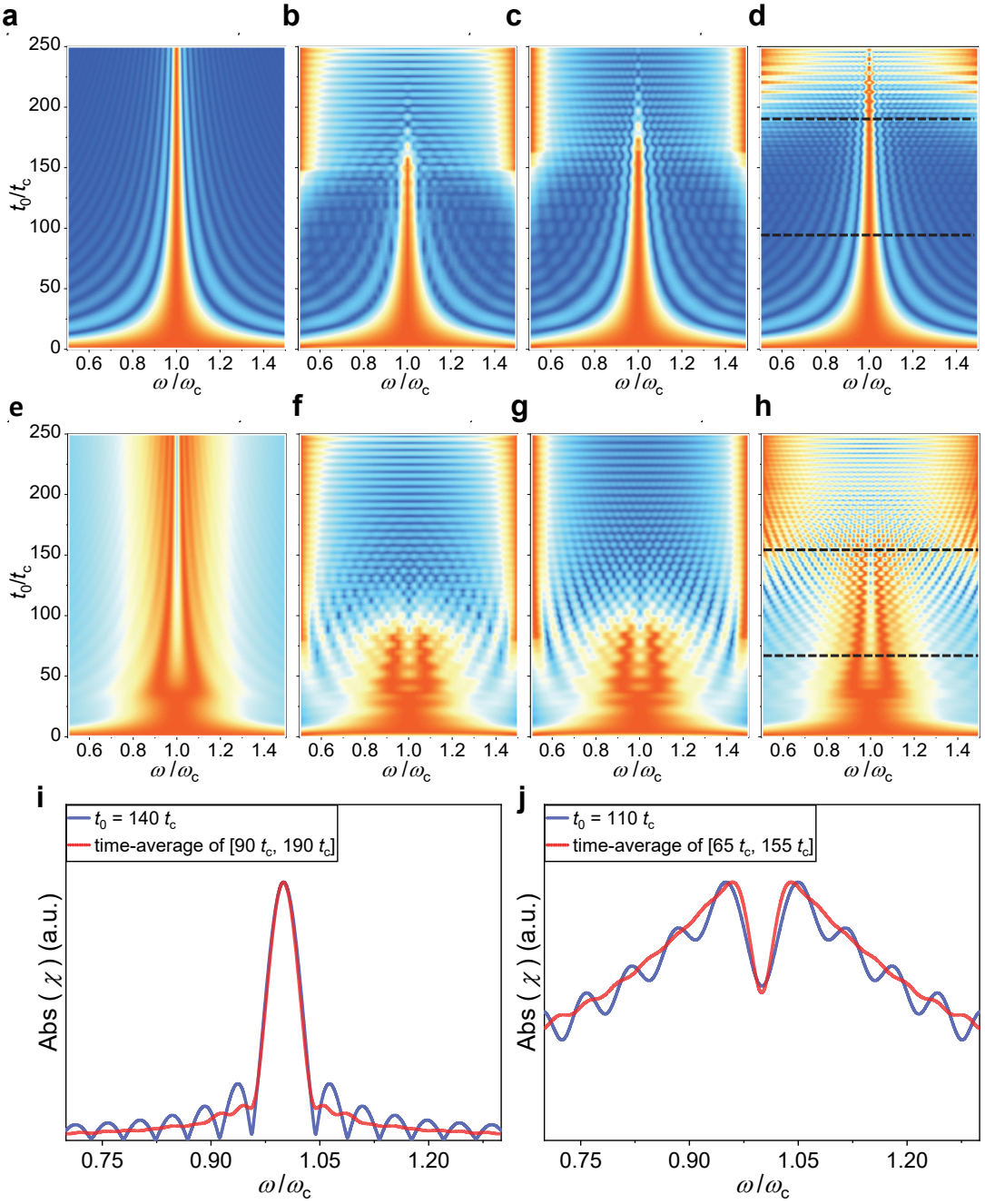

Fig. S1. Effect of time truncation, finite frequency range, and discretization of frequency on the complex frequency spectra of $\chi(\tilde{\omega}, t_0)$ for a single molecular resonance and for coupled system between a single molecular resonance and a plasmonic resonance. (**a-d**) $\chi(\tilde{\omega}, t_0)$ of a molecular system with a single resonance ω_0 with $\gamma = 0.05\,\omega_0$ and $\tau/2 = 0.049\,\omega_0$. (**a**) calculated by equation (S2). (**b**) calculated by equation (2) with $\alpha = 0.5\,\omega_0$, $\beta = 1.5\,\omega_0$ and $\Delta\omega = 0.025\,\omega_0$. (**c**) calculated by equation (2) with $\alpha = 0.5\,\omega_0$, $\beta = 1.5\,\omega_0$ and $\Delta\omega = 0.001\,\omega_0$. (**d**) calculated by equation (2) with $\alpha = 0.2\,\omega_0$, $\beta = 1.8\,\omega_0$ and $\Delta\omega = 0.001\,\omega_0$. (**e-h**)

$\chi(\tilde{\omega}, t_0)$ of a coupling system with $\omega_a = \omega_b = \omega_0$, $\gamma_a = 0.05\,\omega_0$, $\gamma_b = 0.2\,\omega_0$, $\kappa = 0.03\,\omega_0$ and $\tau/2 = 0.049\,\omega_0$. (**e**) calculated by equation (S10). (**f**) calculated by equation (2) with $\alpha = 0.5\,\omega_0$, $\beta = 1.5\,\omega_0$ and $\Delta\omega = 0.025\,\omega_0$. (**g**) calculated by equation (2) with $\alpha = 0.5\,\omega_0$, $\beta = 1.5\,\omega_0$ and $\Delta\omega = 0.001\,\omega_0$. (**h**) calculated by equation (2) with $\alpha = 0.2\,\omega_0$, $\beta = 1.8\,\omega_0$ and $\Delta\omega = 0.001\,\omega_0$. The normalized unit $\omega_c = \omega_0$ and $t_c = 1/\omega_0$. (**i**) Comparison of $\chi(\tilde{\omega})$ at $t_0 = 140\,t_c$ and calculated by the time-average of [$90\,t_c$~$190\,t_c$] (The range between the black dotted lines in (**d**)). (**j**) Comparison of $\chi(\tilde{\omega})$ at $t_0 = 110\,t_c$ and calculated by the time-average of [$65\,t_c$~$155\,t_c$] (The range between the black dotted lines in (**h**)).

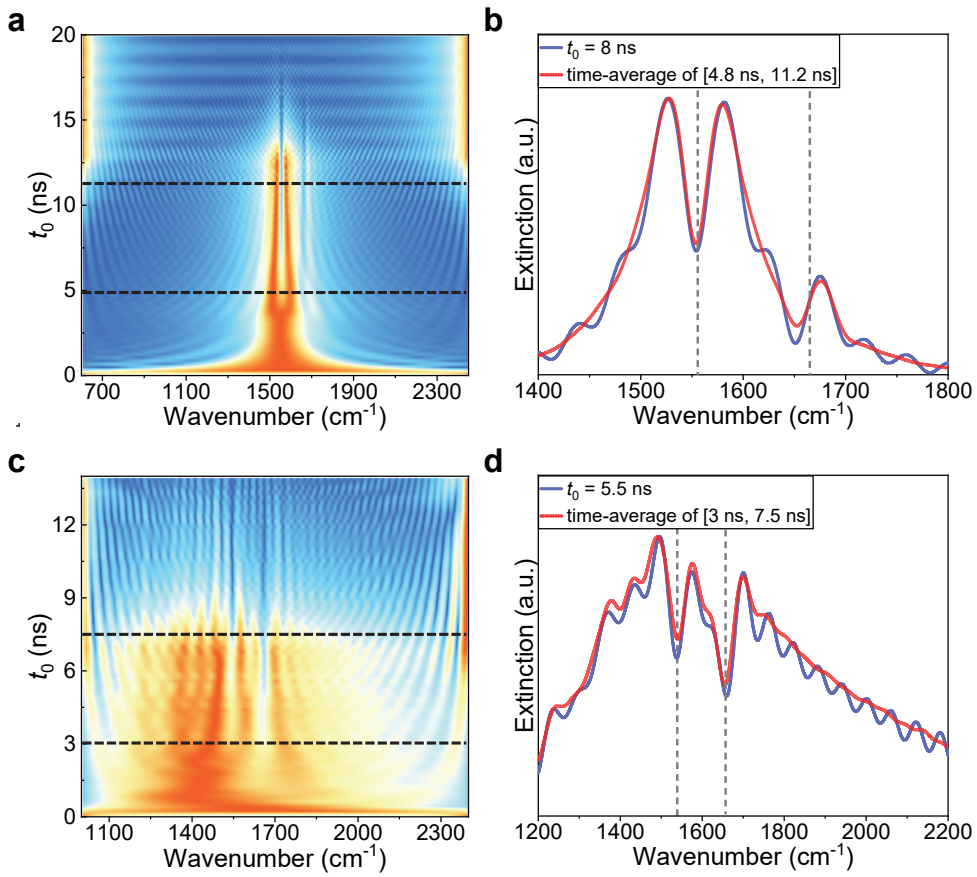

Fig. S2. Effect of time truncation, finite frequency range, and discretization of frequency on the complex frequency spectra of $P(\tilde{\omega})$ for coupled systems consisting of multiple molecular resonances and a single plasmonic resonance, with both numerical and experimental results. (**a**) Spectrum of $P(\tilde{\omega}, t_0)$ calculated by equation (6) for simulation. (**b**) Comparison of $I(\tilde{\omega})$ calculated by $P(\tilde{\omega})$ at $t_0 = 8$ ns and calculated by the time-average of $P(\tilde{\omega})$ [4.8~11.2 ns] (The range between the black dotted lines in (**a**)). The simulation parameters of (**a-b**) are the same as those of Fig. 1c. (**c**) Spectrum of $P(\tilde{\omega}, t_0)$ calculated by equation (6) for the experimental result of ~9-nm-thick BSA protein layer measured by GP-based sensor. (**d**) Comparison of $I(\tilde{\omega})$ calculated by $P(\tilde{\omega})$ at $t_0 = 5.5$ ns and calculated by the time-average of $P(\tilde{\omega})$ [3 ns ~7.5 ns] (The range between the black dotted lines in (**c**)).

Note 2. Phase calculation via Kramers–Kronig relations

In the experiment, only the amplitude spectra are measured. Here we apply Kramers–Kronig relations to recovering the phase $\arg(t_{\mathrm{M}})$ from the amplitude $|t_{\mathrm{M}}|$. Let us consider the general form of Kramers–Kronig relations as follows,

$$\mathrm{Im}(f(x)) = \frac{1}{\pi}\mathcal{P}\int_{\mathbb{R}} \frac{\mathrm{Re}(f(x))}{x - x'}\,\mathrm{d}x' \tag{S11}$$

Equation (S11) tells us how to calculate the imaginary part of $f(x)$ from the real part. In our study, in order to obtain the phase $\arg(t_{\mathrm{M}})$ from the amplitude $|t_{\mathrm{M}}|$, we can define a function that takes the logarithm of t_{M},

$$g(\omega) = \ln\big(t_{\mathrm{M}}(\omega)\big) = \ln|t_{\mathrm{M}}(\omega)| + \mathrm{i}\arg(t_{\mathrm{M}}(\omega)) \tag{S12}$$

According to by equation (S11), we can calculate the imaginary part of $g(\omega)$, that is, the phase $\arg(t_{\mathrm{M}})$ from the real part $\ln|t_{\mathrm{M}}(\omega)|$, which is equation (4) in the maintext. Note that $|t_{\mathrm{M}}(\omega)| \to 1$ as $\omega \to \infty$, such that $\ln|t_{\mathrm{M}}(\omega)| \to 0$ in equation (4). Thus, the integration of Kramers–Kronig relations for $\arg\big(t_{\mathrm{M}}(\omega)\big)$ converges. In Fig. S3b, we compare $\arg\big(t_{\mathrm{M}}(\omega)\big)$ obtained by Kramers–Kronig relations (the red curve) from $|t_{\mathrm{M}}(\omega)|$ (Fig. S3a) and that obtained directly by simulation (the blue curve), which are in good agreement, confirming the validity of equation (4).

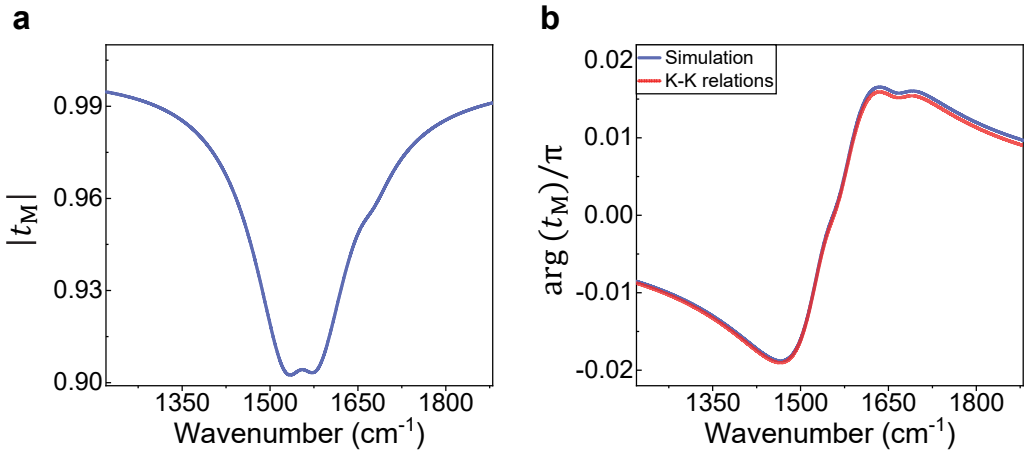

Fig. S3. (**a**) The simulated amplitude $|t_{\mathrm{M}}|$ of the molecular layer attached to GP at real frequency. (**b**) The phase $\arg(t_{\mathrm{M}})$ obtained by Kramers–Kronig relations (the red curve) and by simulation (the blue curve). The simulation parameters of **Fig. S3** are the same as those of Fig. 1c.

Note 3. Enhancing mutiple types of molecular detection

In theory, the synthesized CFW method has potential to applicable to multiple types of molecules, that is, multiple vibration modes. Considering the difference in their damping rates γ_{M}, we need to choose an appropriate value of $\tau/2$, which can simultaneously enhance them. Here we give an example by FEM simulation as shown in Fig. S3, which assumes that there are 3 types of molecules with 4 vibration modes detected by the GP-based sensor. It can be seen that based on the appropriate compensation, all vibration signals are enhanced by the synthesized CFW method.

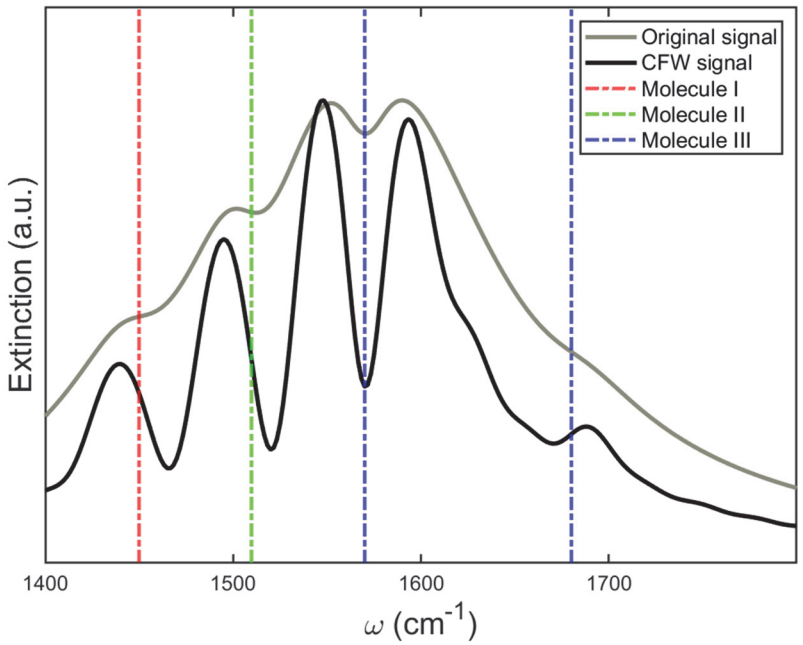

Fig. S4. The extinction spectrum of multiple types of molecules detected by the GP-based sensor at real frequency (the grey curve) and at CFW (the black curve). The parameters of 3 types of molecules as follows: Molecule I with one vibration modes ($\gamma_1 = 50\ \mathrm{cm}^{-1}$, $\omega_{\mathrm{p1}} = 160\ \mathrm{cm}^{-1}$, $\omega_1 = 1450\ \mathrm{cm}^{-1}$); Molecule II with one vibration modes ($\gamma_2 = 40\ \mathrm{cm}^{-1}$, $\omega_{\mathrm{p2}} = 140\ \mathrm{cm}^{-1}$, $\omega_2 = 1510\ \mathrm{cm}^{-1}$); Molecule III with two vibration modes ($\gamma_3 = 30\ \mathrm{cm}^{-1}$, $\omega_{\mathrm{p3}} = 100\ \mathrm{cm}^{-1}$, $\omega_3 = 1570\ \mathrm{cm}^{-1}$, $\gamma_4 = 60\ \mathrm{cm}^{-1}$, $\omega_{\mathrm{p4}} = 120\ \mathrm{cm}^{-1}$, $\omega_4 = 1680\ \mathrm{cm}^{-1}$). We set the temporal attenuation $\tau/2 = 45\ \mathrm{cm}^{-1}$ for all vibration modes.

Note 4. The silk protein on graphene plasmon infrared sensor

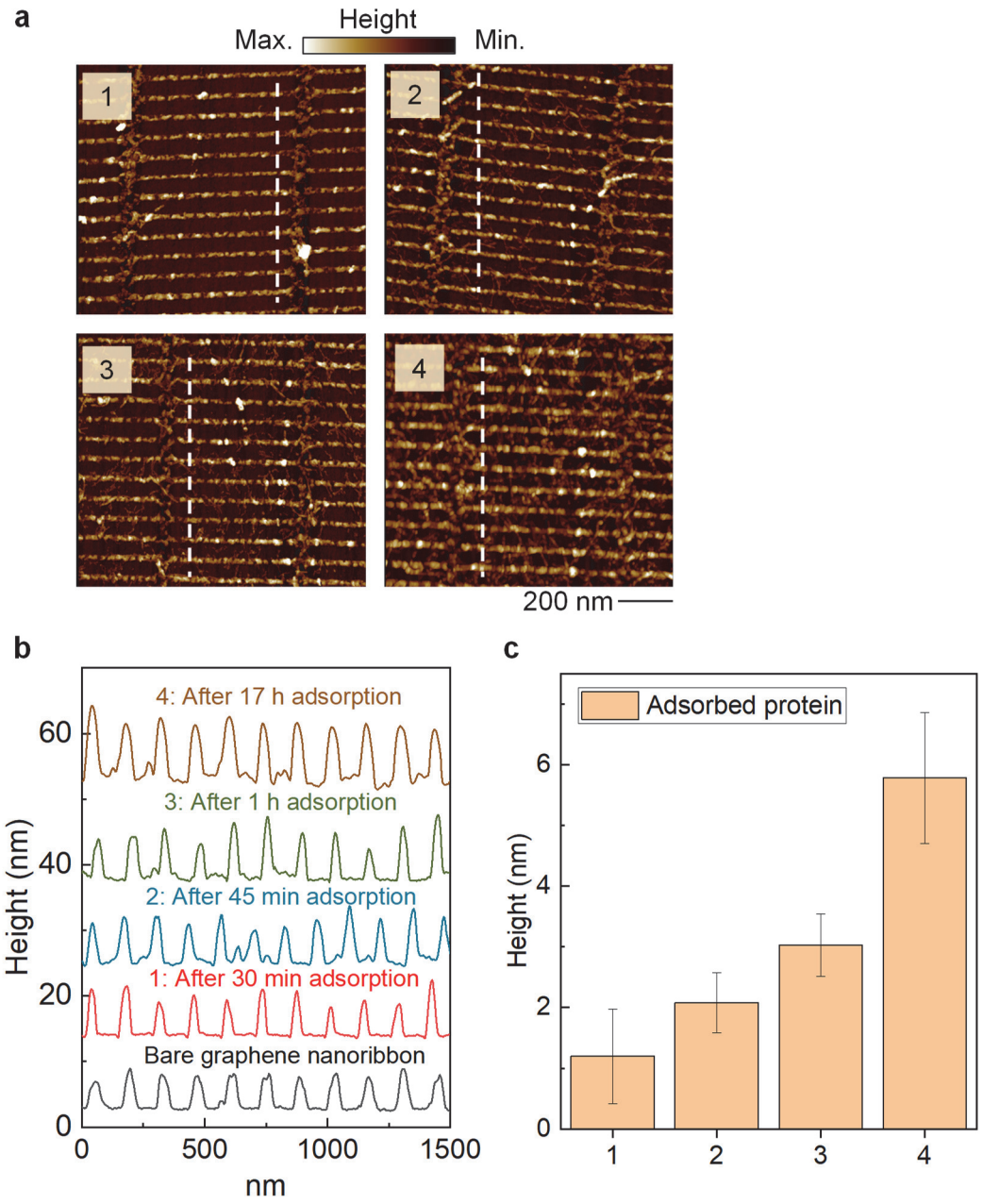

Fig. S5. (a) The morphology of silk protein on graphene nanoribbons when the same graphene plasmon infrared sensor is soaked in silk with different duration. Image 1, 2, 3 and 4 are captured at 30 min, 45 min, 1 h, 17 h, respectively. The roughness (Ra) is 2.1 nm, 2.6 nm, 2.6 nm, 3.5 nm respectively. **(b)** The height profile extracted along the white dashed lines on **(a)**. **(c)** The summarized thicknesses of silk protein, and the average thickness is approximately 1.2 nm , 2.1 nm , 3.0 nm and 5.8 nm , respectively.

Note 5. Characterizing graphene plasmon infrared sensor in aqueous environment

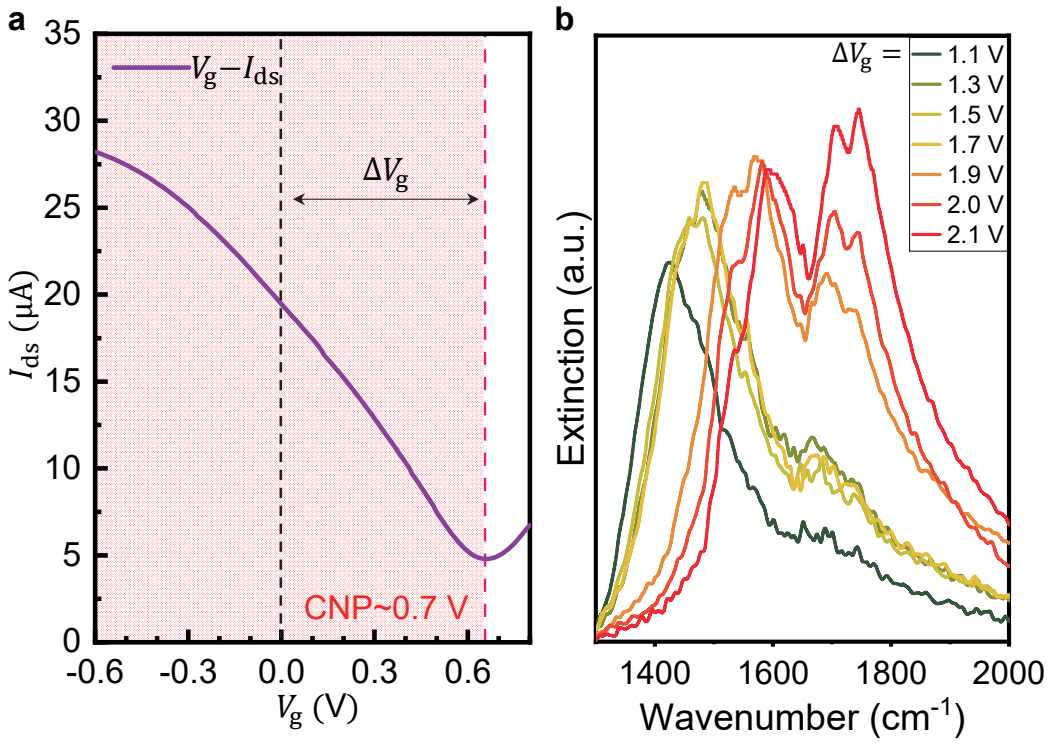

Figure S6. (a) The transfer characterization curve of the graphene plasmon infrared sensor. I_{ds} denotes the current of source and drain. V_g is the gate voltage. The lowest I_{ds} corresponds to the charge neutral point (CNP) which is 0.7 V. **(b)** The original data of extinction spectrum with different ΔV_g ranging from 1.1 V ~ 2.1 V for Fig. 4b-c. The data were collected after 1 mg/mL protein solution flowed for 2 h, with the graphene nanoribbon width $\approx$ 50 nm and the period $\approx$ 120 nm.